Analytical Derivation of the Short-Circuit Current of a Grid-Forming Inverter

Christopher L. Peralta
Department of Electrical and Computer Engineering
Iowa State University
Ames, IA 50011, USA
christ96@iastate.edu

Aboutaleb Haddadi
Deepak Ramasubramanian
Evangelos Farantatos
Electric Power Research Institute, Inc.
Palo Alto, CA 94304 USA
{ahaddadi, dramasubramanian, efarantatos}@epri.com

***Abstract*—The fault response of a grid-forming inverter (GFM) differs from that of a grid-following inverter (GFL) because of their distinct control objectives. The behavior of a GFL during a fault has been extensively studied, and various models are available in commercial fault analysis programs. In contrast, the fault response of a GFM remains less understood, and short-circuit modeling for these inverters is still an active area of research. To address this gap, this paper proposes a mathematical phasor-domain short-circuit model for a GFM operating under a representative fault ride-through (FRT) control and current-limiting scheme. The accuracy of the proposed model is validated through comparison with a detailed electromagnetic transient-type simulation of a GFM. It is important to note that GFM performance is not standardized; numerous FRT and current-limiting implementations exist in the literature, and manufacturer-specific control details are rarely disclosed. This work adopts a commonly referenced GFM FRT and current-limiting approach based on available literature. The proposed model represents an initial step toward developing a comprehensive framework for GFM short-circuit modeling that incorporates diverse control strategies for use in fault analysis programs.**

***Index Terms*—Power system faults, power system protection, renewable energy resources.**

I. Introduction

The fault response of grid-following (GFL) inverter-based resources (IBRs) has been heavily studied [1], [2], and standardized performance requirements are available in the IEEE Standard 2800-2022 [3] and German grid code [4], for instance. However, the behavior of grid-forming (GFM) IBRs under fault conditions is still an active topic of research [5]. Presently, there is no consensus on the most appropriate fault-ride-through (FRT) strategy that would be required from GFM IBRs. Nevertheless, there are ongoing activities addressing this gap, including the UNIFI Consortium [6] and updates to IEEE 2800 series standard, to name a few.

The performance of the GFM IBR related to the impact on protection systems has not been explored in depth [5]. Some efforts have been made to investigate the impacts of GFM IBRs under different FRT strategies on protection elements [7], [8]. However, these efforts have only demonstrated the impacts of GFM IBRs on protection elements through EMT simulations, rather than a rigorous mathematical analysis. Fully understanding the impacts of different FRT strategies for GFM IBRs on protection elements can better support the development of standards describing the required performance of these IBRs during short-circuit faults.

At present, there exist short-circuit models for generic GFL IBRs [9], [10]. For GFM IBRs, however, little work has been done regarding generic equation-based short-circuit models [10]. To the authors' knowledge, no work has been conducted on deriving equation-based short-circuit models for GFM IBR in terms of control parameters, set-points, and pre-fault currents. Hence, a generic equation-based GFM IBR model is needed, specifically relating such terms with the *dq*-axis post-transient positive- and negative-sequence currents.

To this end, this paper has the following objectives:

- (O1): Derive a positive- and negative-sequence equation-based short-circuit model in the *dq*-axis for a generic GFM IBR in [11] using a current saturation technique for current limits. The derived equations are expressed in terms of control parameters, set-points, and pre-fault currents.
- (O2): Showcase the correctness of the derived equations and the dependency of the saturation level in the current saturation on the type of fault and fault location. It was found that the error between the currents obtained with the derived equations and the ones obtained via simulation is less than 10% for all the tested cases. These results are meaningful because the derived equations can be implemented in short-circuit programs. It was also observed that the saturation level of the implemented FRT strategy varies with the type of fault and fault location.

The remainder of the paper is as follows. Section II introduces the positive- and negative-sequence control loop for the generic GFM IBR in [11]. Section III derives the positive- and negative-sequence equation-based short-circuit model in the *dq*-axis for the generic GFM IBR. Section IV develops illustrative case studies to confirm the correctness of the derived equations and the dependency of the saturation level on the type of fault and fault location. Section V concludes.

This material is based upon work supported by the U.S. Department of Energy's Office of Energy Efficiency and Renewable Energy (EERE) under Solar Energy Technologies Office (SETO) Award Number 38637. The views expressed herein do not necessarily represent the views of the U.S. Department of Energy or the United States Government.

979-8-3315-8138-1

II. Grid-Forming Controls

This section provides a succinct explanation of the positive- and negative-sequence control loop for a generic GFM IBR in [11]. Fig. 1a depicts the positive-sequence control loop, and Fig. 1b shows the negative-sequence control loop.

A. Positive-Sequence Multi-Loop Control

Fig. 1a illustrates the positive-sequence multi-loop GFM control as in [11]. The multi-loop control is mainly made up of proportional-integral (PI) current and voltage control loops. The parameters $k_{p,v}$, $k_{p,i}$, $k_{i,v}$, and $k_{i,i}$ are the proportional gains and the integral constants for the voltage and current controllers, respectively. The current control loop regulates the positive-sequence component of $\boldsymbol{i}_{abcf}$ in the *dq*-axis. The transformation matrix used to transform time-domain *abc* quantities into *dq* quantities is:

$$\boldsymbol{K}\left(\theta^{\star}\right)=\frac{2}{3}\begin{bmatrix}\cos\left(\theta^{\star}\right) & \cos\left(\theta^{\star}-2\pi/3\right) & \cos\left(\theta^{\star}+2\pi/3\right)\\ \sin\left(\theta^{\star}\right) & \sin\left(\theta^{\star}-2\pi/3\right) & \sin\left(\theta^{\star}+2\pi/3\right)\end{bmatrix}. \tag{1}$$

The angle $\theta^{\star}$ in (1) is generated by the outer control loop using either the droop control, virtual synchronous machine (VSM), or virtual oscillator (dVOC), q.v. Fig. 1a. The filtered version of the measured *dq*-axis positive-sequence component of $\boldsymbol{i}_{abcf}=[i_{af},i_{bf},i_{cf}]^{\top}$ is labeled as $\boldsymbol{i}^{c}_{dqf,+}=[i^{c}_{df,+},i^{c}_{qf,+}]^{\top}$ in Fig. 1a. The feedforward voltage, $\boldsymbol{v}^{\dagger}_{dqf,+}=[v^{\dagger}_{df,+},v^{\dagger}_{qf,+}]^{\top}$, in the current control is:

$$\boldsymbol{v}^{\dagger}_{dqf,+}=L_f\boldsymbol{i}_{qdf,+}+\boldsymbol{v}_{dqg,+}\ \text{for}\ \boldsymbol{i}_{qdf,+}=[-i_{qf,+},i_{df,+}]^{\top}. \tag{2}$$

In (2), the angular frequency, $\omega^{\star}=d\theta^{\star}/dt$, is neglected as it is considered near rated. In fact, when the frequency freezing option is enabled [11], $\omega^{\star}\approx 1.0$ p.u. $\boldsymbol{i}^{\star}_{dqf,+}=\left[i^{\star}_{df,+},i^{\star}_{qf,+}\right]$ is a saturated version of $\boldsymbol{i}^{*}_{dqf,+}$ which is given by the voltage control. The saturation function $\mathcal{U}$ is:

$$\mathcal{U}\left(\boldsymbol{i}^{*}_{dqf,+},I_{\max,+}\right)=\begin{cases}k_{\text{sat},+}\boldsymbol{i}^{*}_{dqf,+} & \text{if } \|\boldsymbol{i}^{*}_{dqf,+}\|>I_{\max,+}\\ \boldsymbol{i}^{*}_{dqf,+} & \text{otherwise}\end{cases} \tag{3}$$

$$\text{with } k_{\text{sat},+}=\frac{I_{\max,+}}{\left\|\boldsymbol{i}^{*}_{dqf,+}\right\|}. \tag{4}$$

In (4), $I_{\max,+}>0$ is the maximum positive-sequence current magnitude allowed for $\boldsymbol{i}_{abcf}$ in Fig. 1a which given by an adaptive sequence current division block [11].

Furthermore, the voltage control loop generates $\boldsymbol{i}^{*}_{dqf,+}$ such that $\boldsymbol{v}^{\star}_{dqg}=\boldsymbol{v}^{c}_{dqg,+}$ during normal operation. The voltage $\boldsymbol{v}^{\star}_{dqg}=[v^{\star}_{dg},0]^{\top}$ is generated by the outer control loop in Fig. 1a as described in [11], and $\boldsymbol{v}^{c}_{dqg,+}$ is a filter version of the *dq*-axis positive-sequence component of the line-to-neutral voltage $\boldsymbol{v}_{abcg}$. When there is no fault, the voltage control is a PI controller because $v_{\text{frz}}=1$. However, when the fault detector logic detects a fault, $v_{\text{frz}}=0$, making the voltage control only proportional [11]. Further details about the fault detector logic can be found in [11]. The feedforward current, $\boldsymbol{i}^{\dagger}_{dqf,+}$, in the voltage control loop is:

$$\boldsymbol{i}^{\dagger}_{dqf,+}=\omega^{\star}C_f\boldsymbol{v}_{qdg,+}\ \text{for}\ \boldsymbol{v}_{qdg,+}=[-v_{qg,+},v_{dg,+}]^{\top}. \tag{5}$$

B. Negative-Sequence Multi-Loop Control

Fig. 1b presents the negative-sequence control loop in [11]. The current reference, $\boldsymbol{i}^{*}_{dqf,-}$, is generated via the K-factor approach, a shifted version of the measured *dq*-axis negative-sequence voltage $\boldsymbol{v}^{c}_{dqg,-}$. Hence, from Fig. 1b

$$\|\boldsymbol{i}^{*}_{dqf,-}\|=K_{-}\|\boldsymbol{v}^{c}_{dqg,-}\|\ \text{and} \tag{6}$$

$$\texttt{angle}\left(\boldsymbol{i}^{*}_{dqf,-}\right)=\texttt{angle}\left(\boldsymbol{v}^{c}_{dqg,-}\right)-\pi/2 \tag{7}$$

In (6), $K_{-}\in[2,6]$ [12] . The current $\boldsymbol{i}^{*}_{dqf,-}$ is saturated using a function similar to that of (3) to generate $\boldsymbol{i}^{\star}_{dqf,-}$ if $FD=1$ from the fault detector logic [11]; otherwise, $\boldsymbol{i}^{\star}_{dqf,-}=\mathbf{0}$, q.v. Fig. 1b. Hence,

$$\mathcal{U}\left(\boldsymbol{i}^{*}_{dqf,-},I_{\max,-}\right)=\begin{cases}k_{\text{sat},-}\boldsymbol{i}^{*}_{dqf,-} & \text{if } \|\boldsymbol{i}^{*}_{dqf,-}\|>I_{\max,-}\\ \boldsymbol{i}^{*}_{dqf,-} & \text{otherwise}\end{cases} \tag{8}$$

$$\text{with } k_{\text{sat},-}=\frac{I_{\max,-}}{\left\|\boldsymbol{i}^{*}_{dqf,-}\right\|}. \tag{9}$$

In (9), $I_{\max,-}\geq 0$ is given by an adaptive sequence current division block [11] as $I_{\max,+}$ in (4), and $\|\boldsymbol{i}^{*}_{dqf,-}\|$ is from (6). Because the saturation function in (8) only changes the current reference magnitude, $\texttt{angle}\left(\boldsymbol{i}^{\star}_{dqf,-}\right)=\texttt{angle}\left(\boldsymbol{i}^{*}_{dqf,-}\right)$ where the right-hand-side term is from (7). For negative-sequence current control control in Fig. 1b, the feedforward voltage, $\boldsymbol{v}^{\dagger}_{dqf,-}$, is expressed as

$$\boldsymbol{v}^{\dagger}_{dqf,-}=L_f\boldsymbol{i}_{qdf,-}+\boldsymbol{v}_{dqg,-}\ \text{for}\ \boldsymbol{i}_{qdf,-}=[i_{qf,-},-i_{df,-}]^{\top}. \tag{10}$$

III. Equation-Based Short-Circuit Model

This section develops equations to describe the *dq*-axis post-transient positive- and negative-sequence short-circuit currents injected by the GFM IBR in Section II to the grid when implementing the current saturation. The model of the adaptive sequence current division block in [11] is not considered. To this end, the dynamic of the positive-sequence line-to-neutral voltage across C_f in the *dq*-axis using $\boldsymbol{K}(\theta)$ of (1) is given:

$$C_f\frac{d\boldsymbol{v}_{dqg,+}}{dt}=\boldsymbol{i}_{dqf,+}-\boldsymbol{i}_{dqg,+}-\omega C_f\boldsymbol{v}_{qdg,+}. \tag{11}$$

In (11), $\boldsymbol{v}_{qdg,+}=[-v_{qg,+},v_{dg,+}]^{\top}$. Equation (11) is used in the following subsection to develop expressions that characterize the *dq*-axis post-transient positive-sequence current injection by the GFM IBR in Section II.

A. Positive-Sequence Short-Circuit Current

Because the dc-link voltage is at rated value, and the current control in Fig. 1 remains PI when the IBR is subjected to a fault, it is considered here that $\boldsymbol{i}^{c}_{dqf,+}=\boldsymbol{i}^{\star}_{dqf,+}$. As explained in Section II-A, the integral part of the PI voltage control is disabled via v_{frz}, causing that $\boldsymbol{i}^{*}_{dqf,+}$ during fault depends on the pre-fault $\boldsymbol{i}^{*}_{dqf,+}$. Considering no saturation before the fault occurs, $\boldsymbol{i}^{\star}_{dqf,+}(t=0^{-})=\boldsymbol{i}^{*}_{dqf,+}(t=0^{-})$, and assuming $\boldsymbol{z}_{dq,i}(t=0^{-})\gg\boldsymbol{i}^{\dagger}_{dqf,+}(t=0^{-})$ because of the value of C_f,

$$\boldsymbol{i}^{*}_{dqf,+}\left(t=0^{-}\right)\approx\boldsymbol{i}^{c}_{dqg,+}\left(t=0^{-}\right)\approx\boldsymbol{z}_{dq,i}\left(t=0^{-}\right). \tag{12}$$

979-8-3315-8138-1

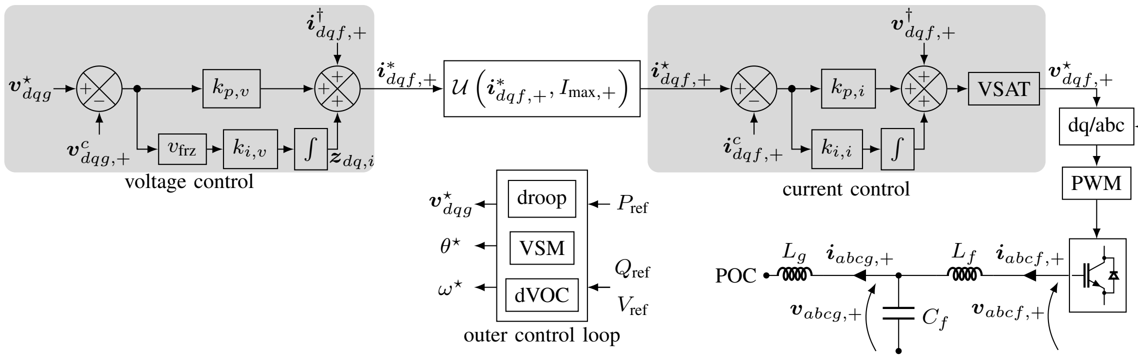

(a) positive-sequence control loop

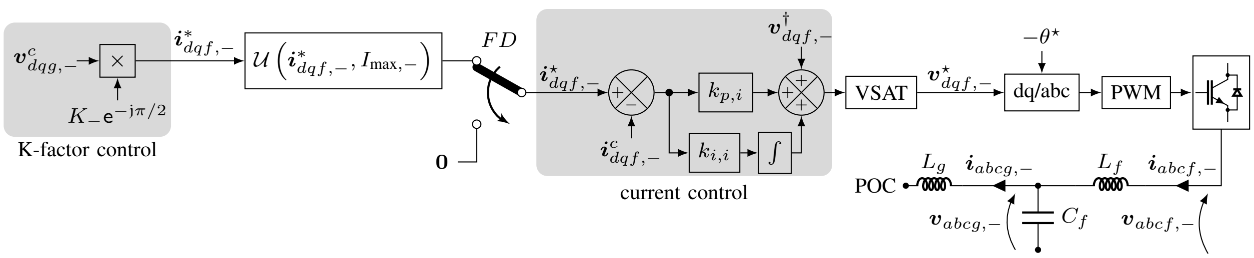

(b) negative-sequence control loop

Fig. 1. Generic multi-loop GFM control from [11].

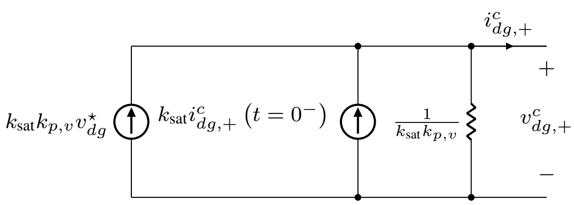

(a) d-axis equivalent circuit

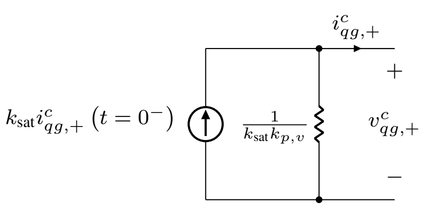

(b) q-axis equivalent circuit

Fig. 2. Equivalent circuit in the positive-sequence network.

Hence, using (12), $\boldsymbol{i}^{*}_{dqf,+}(t>0)$ is computed as follows

$$\boldsymbol{i}^{*}_{dqf,+}(t>0) \approx k_{p,v}\left(\boldsymbol{v}^{\star}_{dqg} - \boldsymbol{v}^{c}_{dqg,+}(t>0)\right) + \boldsymbol{i}^{c}_{dqg,+}\left(t=0^{-}\right). \quad (13)$$

In (13), $\boldsymbol{i}^{\dagger}_{dqf,+}(t>0)$ of (5) is neglected. Because $\boldsymbol{i}^{\star}_{dqf,+}(t>0)$ is a saturated version of $\boldsymbol{i}^{*}_{dqf,+}(t>0)$ via (3), the effect of C_f on (11) is neglected, and it is assumed the steady-state condition of (11),

$$\boldsymbol{i}^{c}_{dqg,+}(t>0) \approx k_{\mathrm{sat},+}k_{p,v}\left(\boldsymbol{v}^{\star}_{dqg} - \boldsymbol{v}^{c}_{dqg,+}(t>0)\right) + k_{\mathrm{sat},+}\boldsymbol{i}_{dqg,+}\left(t=0^{-}\right) \quad (14)$$

where $k_{\mathrm{sat},+}$ is from (4) and depends on the magnitude of $\boldsymbol{i}^{*}_{dqf,+}$ of (13). In (14), neither $k_{\mathrm{sat},+}$ nor $\boldsymbol{v}^{c}_{dqg,+}$ is controllable. The Norton-equivalent circuits in Fig. 2 represent (14). The current $i^{c}_{dg,+}$ depends on the set-point voltage $v^{\star}_{dg}$, the pre-fault current $i^{c}_{dg,+}(t=0^{-})$, and the terminal voltage $v^{c}_{dg,+}$. However, $i^{c}_{qg,+}$ depends only on the pre-fault current $i^{c}_{qg,+}(t=0^{-})$ and the terminal voltage $v^{c}_{qg,+}$, considering $v^{\star}_{qg}=0$.

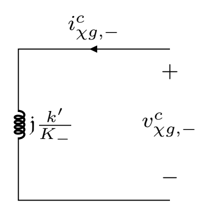

Fig. 3. Negative-sequence equivalent circuit where $\chi \in \{d,q\}$.

B. Negative-Sequence Short-Circuit Current

Because the negative-sequence current control remains as a PI control during short-circuit faults, it is assumed that this control loop makes $\boldsymbol{i}^{\star}_{dqf,-} = \boldsymbol{i}^{c}_{dqf,-}$. Thus, considering (6) and (7) and neglecting the effect of C_f,

$$\boldsymbol{i}^{c}_{dqg,-} \approx k' K_{-} \boldsymbol{v}^{c}_{dqg,-} \mathrm{e}^{-\mathrm{j}\pi/2} \quad (15)$$

$$\text{with } k' = \begin{cases} k_{\mathrm{sat},-} & \text{if } \|\boldsymbol{i}^{*}_{dqf,-}\| > I_{\max,-} \\ 1 & \text{otherwise} \end{cases} \quad (16)$$

$$\text{and } \boldsymbol{i}^{*}_{dqf,-} = K_{-}\boldsymbol{v}^{c}_{dqg,-}\mathrm{e}^{-\mathrm{j}\pi/2}. \quad (17)$$

Equation (15) is valid only if $FD=1$, q.v. Fig. 1b. Because k' depends on $\boldsymbol{v}^{c}_{dqg,-}$, k' is uncontrollable as $k_{\mathrm{sat},+}$ of (4). An equivalent circuit from (15) is depicted in Fig. 3.

IV. Case Study

The case study considers a modified IEEE 39-bus grid of Fig. 4 which is implemented in PSCAD V5.0.2. The simulation time step is $1.0\,\mu$s, and the simulation duration is 22.0 s.

979-8-3315-8138-1

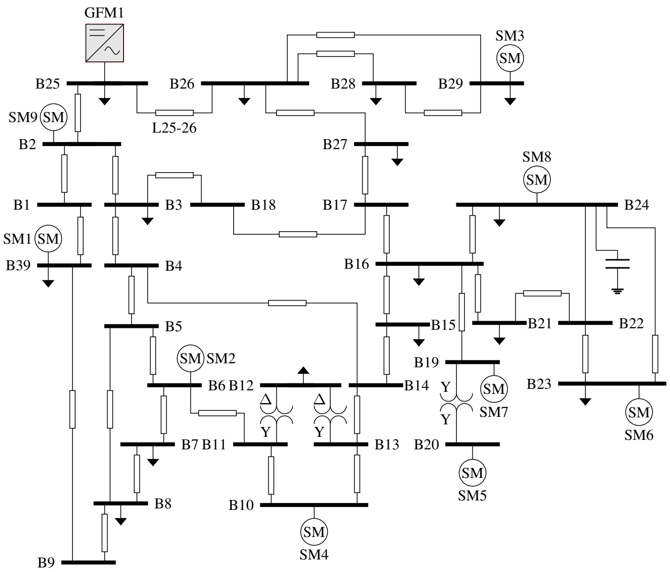

Fig. 4. Modified IEEE 39-bus system.

TABLE I
GFM IBR PARAMETERS

par.	val.	unit	par.	val.	unit
$k_{p,v}$	5.0	p.u.	$k_{i,v}$	30.0	p.u.
$k_{p,i}$	2.0	p.u.	$k_{i,i}$	20.0	p.u.
K_{-}	6.0	p.u.	$I_{\max}$	1.3	p.u.

A 540-MVA/345-kV GFM IBR-based power plant at B25 is made up by aggregating five hundred forty 1.0-MVA/0.65-kV fully-rated GFM IBR. The dc-link voltage is considered stiff. The GFM IBR parameters are shown in Table I; $I_{\max}$ is the maximum allowed current magnitude which is used to compute $I_{\max,+}$ in (4) and $I_{\max,-}$ in (9). The angle $\theta^{\star}$ is generated by the speed-droop law using 2.0% droop constant. The frequency freezing is enabled. Here, it is considered reactive power priority. Several bolted faults are applied in L25-26 and B26 of Fig. 4. This line is 102.4-km long and has a positive-and zero-sequence impedances of $38.61\angle 85.21°\,\Omega$ and $80.62\angle 80.73°\,\Omega$. A subset of results is shown in Figs. 7–6 and Table II. All faults are applied at $t = 20.0\,$s.

A. Case I: Positive- and Negative-Sequence Current Injection

Fig. 5 depicts $\boldsymbol{v}^{c}_{dqg,+}$, $\boldsymbol{v}^{c}_{dqg,-}$, $\boldsymbol{i}^{c}_{dqg,+}$, and $\boldsymbol{i}^{c}_{dqg,-}$ for GFM1 under the current saturation approach at B25 in Fig. 4 when a bolted AG fault occurs in L25-26 at 20 km from B25. From Fig. 5a, one can learn: (A) $v^{c}_{dg,+} = 0.73\,$p.u. at $t = 20.08\,$s. (B) $v^{c}_{qg,+} = 0.044\,$p.u. at $t = 20.08\,$s. The voltage $\boldsymbol{v}^{c}_{dqg,+}$ settled by $t = 20.08\,$s. (C) $i^{c}_{dg,+}(t = 20^{-}) = 0.96\,$p.u. (D) $i^{c}_{qg,+}(t = 20^{-}) = 0.029\,$p.u. (E) At $t = 20.08\,$s, $i^{c}_{dg,+} = 1.12\,$p.u. (F) At $t = 20.08\,$s, $i^{c}_{qg,+} = -0.10\,$p.u. The current $\boldsymbol{i}^{c}_{dqg,+}$ starts settling after $t = 20.08\,$s. By substituting $\boldsymbol{v}^{c}_{dqg,+}$ at $t = 20.08\,$s, $\boldsymbol{i}^{c}_{dqg,+}(t = 20^{-})$, $k_{p,v} = 5.0$ from Table I, and $k_{\text{sat}} = 0.48$ from Fig. 7 into (14), $i^{c}_{dg,+} \approx 1.11\,$p.u. and $i^{c}_{qg,+} \approx -0.092\,$p.u., having errors of 0.9% and 8.0%, respectively, with respect to the simulated values. Hence, these results suggest that (14) gives an acceptable approximation to $\boldsymbol{i}^{c}_{dqg,+}$. From Fig. 5b, one can learn: (A) At $t = 20.08\,$s, $v^{c}_{dg,-} = 0.18\,$p.u. (B) $v^{c}_{qg,-} = -0.16\,$p.u. at $t = 20.08\,$s. (C) At $t = 20.08\,$s, $i^{c}_{dg,-} = -0.12\,$p.u. (D) $i^{c}_{qg,-} = -0.13\,$p.u. at $t = 20.08\,$s. Because $\boldsymbol{i}^{\star}_{dqf,-}$ is computed using the K-factor approach, $\boldsymbol{i}^{\star}_{dqf,-}$ varies as $\boldsymbol{v}^{c}_{dqg,-}$ changes. By using the previous voltage values, $k' = 0.13\,$p.u., and (15), $i^{c}_{dg,-} \approx -0.12\,$p.u. and $i^{c}_{qg,-} \approx -0.13\,$p.u. from Fig. 8 at $t = 20.08\,$s. From these results, one can infer that (15)–(17) give acceptable results.

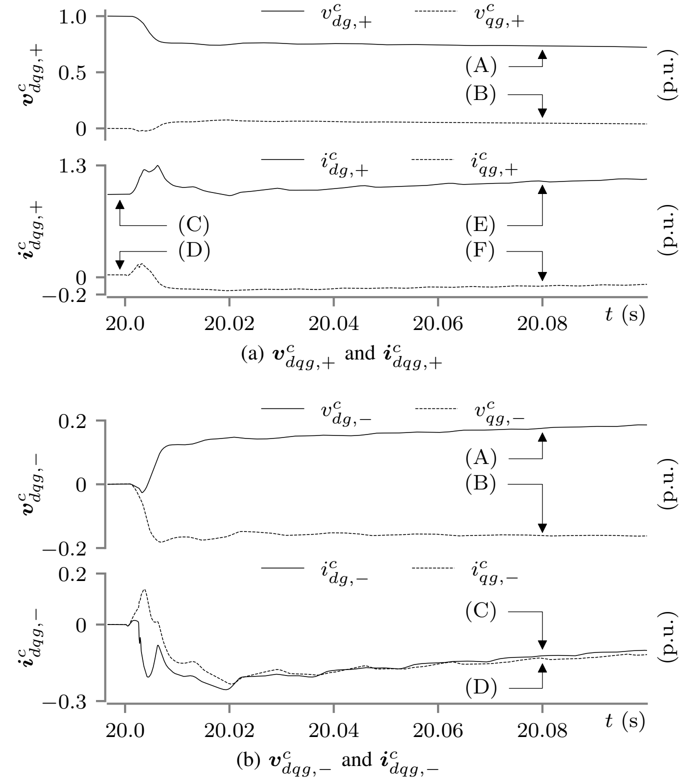

(a) $\boldsymbol{v}^{c}_{dqg,+}$ and $\boldsymbol{i}^{c}_{dqg,+}$

(b) $\boldsymbol{v}^{c}_{dqg,-}$ and $\boldsymbol{i}^{c}_{dqg,-}$

Fig. 5. $\boldsymbol{v}^{c}_{dqg,+}$, $\boldsymbol{v}^{c}_{dqg,-}$, $\boldsymbol{i}^{c}_{dqg,+}$, and $\boldsymbol{i}^{c}_{dqg,-}$ for a bolted AG fault in L25-25 at 20 km from B25 in Fig. 4.

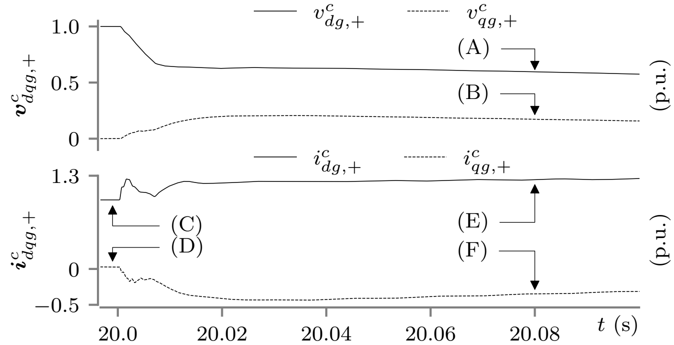

Fig. 6. $\boldsymbol{v}^{c}_{dqg,+}$ and $\boldsymbol{i}^{c}_{dqg,+}$ for a bolted-symmetrical fault at B26.

Fig. 6 presents $\boldsymbol{v}^{c}_{dqg,+}$ and $\boldsymbol{i}^{c}_{dqg,+}$ for GFM1 under the current saturation at B25 in Fig. 4 when a bolted-symmetrical (ABCG) fault occurs at B26. Because the fault is symmetric, the GFM IBR does not inject negative-sequence current. From Fig. 6, one can learn: (A) At $t = 20.08\,$s, $v^{c}_{dg,+} = 0.59\,$p.u. (B) $v^{c}_{qg,+} = 0.17\,$p.u. at $t = 20.08\,$s. (C) Just before the fault occurs, $i^{c}_{dg,+} = 0.96\,$p.u. (D) $i^{c}_{qg,+} = 0.029\,$p.u. just prior to the fault. (E) At $t = 20.08\,$s, $i^{c}_{dg,+} = 1.24\,$p.u. (F) $i^{c}_{qg,+} = -0.35\,$p.u. The current $\boldsymbol{i}^{c}_{dqg,+}$ only experiences small changes after $t = 20.08\,$s. Using $\boldsymbol{v}^{c}_{dqg,+}$ at $t = 20.08\,$s, $\boldsymbol{i}^{c}_{dqg,+}(t = 20^{-})$, $k_{p,v} = 5.0$, and $k_{\text{sat}} = 0.41$ from Fig. 7,

979-8-3315-8138-1

TABLE II

SUMMARY TABLE

fault	$i^c_{dg,+}$	$i^c_{qg,+}$	$v^c_{dg,+}$	$v^c_{qg,+}$	$i^c_{dg,-}$	$i^c_{qg,-}$	$v^c_{dg,-}$	$v^c_{qg,-}$	$k_{\text{sat},+}$	k'
AG	1.12	-0.10	0.73	0.044	-0.12	-0.13	0.18	-0.16	0.48	0.13
ABCG	1.24	-0.35	0.59	0.17	0.0	0.0	0.0	0.0	0.41	0.0

The values are in per-unit and are taken at $t = 20.08$ s.

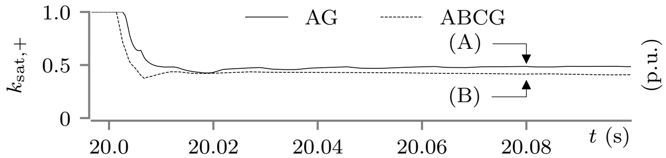

Fig. 7. $k_{\text{sat},+}$ of (4) for a bolted AG fault in L25-26 at 20 km from B25 and a bolted-symmetrical fault at B26.

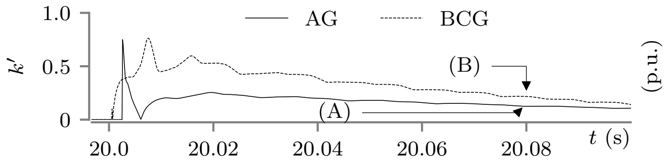

Fig. 8. k' of (16) for a bolted AG fault in L25-26 at 20 km from B25 and a bolted BCG fault at the middle of L25-26.

and (14), $i^c_{dg,+} \approx 1.24$ p.u. and $i^c_{qg,+} \approx -0.34$ p.u., having errors of 0.0% and 2.9% with respect to the simulated values. A summary of the results in Figs. 5–8 is shown in Table II.

Overall, one can infer that (14) gives an acceptable approximation to $\boldsymbol{i}^c_{dqg,+}$ when the GFM IBR under current saturation is subjected to symmetrical and asymmetrical short-circuit faults. The error between the estimated and simulated currents is less than 10%. The same can be said for the approximation of $\boldsymbol{i}^c_{dqg,-}$. Therefore, the equivalent circuits shown in Figs. 2 and 3 can be implemented in short-circuit software to represent the positive- and negative-sequence behavior of the generic GFM IBR in [11] under the current saturation.

B. Case II: Dependency of the Saturation Level on the Type of Fault and Fault Location

Fig. 7 illustrates $k_{\text{sat},+}$ of (4) for a bolted AG fault in L25-26 at 20 km from B25 and a bolted-symmetrical fault at B26. At $t = 20.08$ s: (A) $k_{\text{sat},+} = 0.48$ p.u for the AG fault. (B) $k_{\text{sat},+} = 0.41$ p.u. for the symmetrical fault. The difference between $k_{\text{sat},+}$ for different types of faults at different locations is because of the influence of $\boldsymbol{v}^c_{dqg,+}$ as explained in Section III-A. For the AG fault, $\boldsymbol{v}^c_{dqg,+} = [0.73, 0.044]^\top$ p.u. at $t = 20.08$ s, q.v. Fig. 5a, while $\boldsymbol{v}^c_{dqg,+} = [0.59, 0.17]^\top$ p.u., q.v. Fig. 6, for the symmetrical fault.

Fig. 8 shows k' of (16) for a bolted AG fault in L25-26 at 20 km from B25 and a bolted BCG fault at the middle of L25-26. From Fig. 8, one can learn: (A) $k' = 0.13$ p.u. at $t = 20.08$ s for the AG fault. (B) At $t = 20.08$ s, $k' = 0.22$ p.u. for the BCG fault. As for $k_{\text{sat},+}$, k' varies with the type of fault and location as it depends on $\boldsymbol{v}^c_{dqg,-}$.

Overall, the results suggest that $k_{\text{sat},+}$ of (4) and k' of (3) are uncontrollable because they depend on how the type of fault and fault location impact $\boldsymbol{v}^c_{dqg,+}$ and $\boldsymbol{v}^c_{dqg,-}$, respectively. This, in turn, makes the *dq*-axis the positive- and negative-sequence currents uncontrollable. Hence, the *dq*-axis current components are tied to the type of fault and fault location.

V. Conclusion

This paper has developed a *dq*-axis positive- and negative-sequence equation-based short-circuit model for the generic GFM IBR in Section II. For the considered cases in Section IV, the estimated currents using the derived equations acceptably matched the values obtained from EMT simulations for asymmetrical and symmetrical faults. Furthermore, it was also explained in Sections III-A and III-B and showcased in Section IV-B the dependency of the saturation level in the current saturation on the terminal voltage which, in turn, depends on the type of fault and fault location.

The findings herein suggest that the equation-based short-circuit models derived in Section III fairly represent the post-transient short-circuit behavior of the generic GFM IBR. Hence, these models can be implemented in short-circuit programs. Future work will model the adaptive sequence current division block and consider other fault-ride-through strategies such as virtual impedance, hybrid, and voltage limiting.

References

[1] A. Azizi, A. Banaiemoqadam, A. Hooshyar, and M. Patel, "A blind spot in the LVRT current requirements of modern grid codes for inverter-based resources," *IEEE Trans. Power Del.*, vol. 38, no. 1, pp. 319–334, Feb. 2023.

[2] Y. Chang, I. Kocar, E. Farantatos, A. Haddadi, and M. Patel, "Short-circuit modeling of DFIG-based WTG in sequence domain considering various fault-ride-through requirements and solutions," *IEEE Trans. Power Del.*, vol. 38, no. 3, pp. 2088–2100, Jun. 2023.

[3] *IEEE Standard for Interconnection and Interoperability of Inverter-Based Resources (IBRs) Interconnecting with Associated Transmission Electric Power Systems*, IEEE Std 2800-2022, Apr. 2022.

[4] "Technical Requirements for the Connection and Operation of Customer Installations to the Extra High Voltage Network (TAR Extra High Voltage)," Berlin, Germany, Tech. Rep. VDE-AR-N 4130, Nov. 2018. [Online]. Available: https://www.vde.com/en/fnn/topics/technical-connection-rules/tcr-extra-high-voltage

[5] U. Münz *et al.*, "Protection of 100% inverter-dominated power systems with grid-forming inverters and protection relays - gap analysis and expert interviews," Sandia National Labs, Alburquerque, NM, USA, Tech. Rep. SAND2024-04848, Apr. 2024.

[6] UNIFI Consortium, "UNIFI Specifications for Grid-Forming Inverter-Based Resources – Version 2," Tech. Rep. UNIFI-2024-2-1, Mar. 2024.

[7] N. Baeckeland, D. Venkatramanan, S. Dhople, and M. Kleemann, "On the distance protection of power grids dominated by grid-forming inverters," in *Proc. IEEE PES Innovative Smart Grid Technol. Conf. Europe*, Novi Sad, Serbia, Oct. 10–12 2022.

[8] C. L. Peralta and H. N. Villegas Pico, "Impact of grid-forming converters on distance elements based on the X and M calculations," in *Proc. 2024 IEEE Texas Power and Energy Conf.*, College Station, TX, USA, Feb. 12–13.

[9] Z. Cheng *et al.*, "Assessing inverter-based resources modeling gaps in commonly used short-circuit programs," in *Proc. 78th Ann. Conf. Protective Relay Engineers*, College Station, TX, USA, Feb. 31– Apr. 03 2025.

[10] X. Chen, A. Haddadi, Z. Yang, E. Farantatos, and I. Kocar, "Efficient, robust, and comprehensive fault calculation of IBR-rich systems considering diverse controls," *IEEE Open Access J. Power and Energy*, vol. 12, pp. 378–390, Jun. 2025.

[11] *Generic Grid Forming (GNRGFM) Model - PSCAD v1.0 — Technical Update*, Electric Power Research Institute, EPRI, Palo Alto, CA, Dec. 2025.

[12] A. Haddadi, I. Kocar, J. Mahseredjian, U. Karaagac, and E. Farantatos, "Negative sequence quantities-based protection under inverter-based resources – Challenges and impact of the German grid code," *Electric Power Syst. Res.*, vol. 188, p. 106573, Nov. 2020.